Laser-enhanced magnetism in SmFeO₃

Mohsen Yarmohammadi [1,*] Marin Bukov [2,†] Vadim Oganesyan,[3,4,5,‡] and Michael H. Kolodrubetz [1,§]

[1]*Department of Physics, The University of Texas at Dallas, Richardson, Texas 75080, USA*
[2]*Max Planck Institute for the Physics of Complex Systems, Nöthnitzer Str. 38, 01187 Dresden, Germany*
[3]*Physics Program and Initiative for the Theoretical Sciences, The Graduate Center, CUNY, New York, New York 10016, USA*
[4]*Center for Computational Quantum Physics, Flatiron Institute, 162 5th Avenue, New York, New York 10010, USA*
[5]*Department of Physics and Astronomy, College of Staten Island, CUNY, Staten Island, New York 10314, USA*

We investigate the coherent enhancement of inherently weak magnetic interactions in rare-earth orthoferrite SmFeO₃ as a functional material for spintronic applications using a realistic model of dissipative spin dynamics that are linearly and quadratically coupled to laser-driven infrared-active phonons. When linear coupling dominates, we discover a magnetophononic dynamical first-order phase transition in the nonequilibrium steady state which can inhibit strong enhancement of magnetic interactions. By contrast, when quadratic spin-phonon coupling dominates, no phase transition exists at experimentally relevant parameters. By utilizing a chirp protocol, the phase transition can be engineered, enabling stronger magnetic interactions. We also discuss the route for experimental observation of our results.

I. INTRODUCTION

In recent years, the prospect of using spins as alternative information carriers has led to the emerging field of spintronics, which promises next-generation digital processing units that are fast, robust, and energy efficient [1]. In solid materials exhibiting magnetic properties, the electronic spins interact with lattice vibrations (phonons) opening up a back-action channel, through electron orbital hybridization.

The famous magnetic material class whose role in spintronics is as significant as silicon in electronics is the rare-earth orthoferrites (perovskite oxides) RXO_3, with magnetic rare-earth ion R and a magnetic ion X [2]. A primary example is SmFeO₃, where at low temperatures an unusually strong nonlinear spin-phonon coupling (SPC) arises from the crosstalk between the two magnetic iron and samarium ions [3], in contrast to most examples that deal only with one magnetic lattice and linear SPC.

Even though the nonlinear SPC in SmFeO₃ is strong, the magnetic exchange interactions including Sm spins are weak [4]. While various Sm-magnetic orders have been reported to explore the interplay between phonons, spin-orbit coupling, and Sm magnetism, the precise Sm-spin ordering is still unclear. Enhancing these interactions will enhance the effects controlled by the unusual nonlinear SPC. This is necessary to leverage their unusually large spin interactions for the design of material properties from a scientific perspective, as they exhibit intriguing features such as the measurable

magnetoelectric effect [5–9], and for applications in industry, e.g., in solar cells and spintronics [10–12].

A conventional way is to apply pressure [13] or magnetic field [14]. In contrast to these static approaches, dynamic control techniques emerge as a new frontier to induce and observe a broader array of novel phenomena that only exist away from equilibrium [15–17]. Since spin motions in solids typically have a timescale that coincides with the THz spectrum region, detection and manipulation of spins by optical means is indispensable.

In this paper, we propose a nonequilibrium magnetophononic mechanism to manipulate inherent weak spin-spin interactions in SmFeO₃ via laser-driven single-mode infrared-active (IR-active) phonons that play the central role of a mediator for dynamic control of spins. The term magnetophononics was originally coined in the context of classical magnets [18]. However, in this work, we adapt the magnetophononic protocol to a quantum spin system featuring quantum dissipation. We first show that magnetic interactions are enhanced in SmFeO₃ for the on-resonance laser-phonon coupling regime. More importantly, we discover a dynamical magnetophononic first-order phase transition in SmFeO₃ in the off-resonance laser-phonon coupling regime to be a more efficient way to further enhance magnetism as compared to the on-resonance one. We also discuss the origin of the transition from inherent nonlinearities in the mechanism as well as a feasible solution in the experiment to observe these phenomena. Finally, we propose a linear chirp drive to further enhance the magnetic response of the system.

This paper is structured as follows: Section II introduces the Hamiltonian model describing SmFeO₃ at low temperatures, an anisotropic antiferromagnetic spin $S = \frac{5}{2}$ chain. Subsequently, we compute the time evolution of all observables. In Sec. III, we present the primary findings and results

*Contact author: mohsen.yarmohammadi@utdallas.edu
†Contact author: mgbukov@pks.mpg.de
‡Contact author: vadim.oganesyan@csi.cuny.edu
§Contact author: mkolodru@utdallas.edu

obtained for various parameter sets. Additionally, we briefly discuss the relevance of these phenomena to experimental measurements in Sec. IV. Finally, Sec. V summarizes the paper.

II. MODEL

We consider $SmFeO_3$ at extremely low temperatures, where the weak spin interaction between Sm^{3+} and Fe^{2+} ions can be effectively described by an anisotropic antiferromagnetic (AFM) Heisenberg $S = \frac{5}{2}$ chain (XXZ model) [3,4,19,20]. Vibrational modes are initially excited by a THz continuous wave laser, inducing a coherent phonon field on every site ℓ. This field couples both linearly and quadratically to the nearest isotropic (in-plane) and anisotropic (easy-axis) spin interactions [21–24]. It is important to note that our considerations pertain only to the phonon we drive, given the plethora of phonons in the spectrum. Despite the minimal complexity of our model for a magnetophononically driven quantum spin system, it encompasses all essential components to capture the fundamental physics of real-driven materials. Therefore, the total Hamiltonian governing the dynamics comprises four terms:

$$\mathcal{H} = \mathcal{H}_s + \mathcal{H}_{ph} + \mathcal{H}_{sp} + \mathcal{H}_{lp}, \quad (1)$$

with

$$\mathcal{H}_s = \sum_{\langle \ell, j \rangle} \left(J \left[S_\ell^x S_j^x + S_\ell^y S_j^y \right] + J \Delta S_\ell^z S_j^z \right). \quad (2)$$

The in-plane isotropic exchange coupling is approximately $J \simeq 0.1\,\text{meV}$, while the phenomenological anisotropic AFM parameter Δ is greater than 1 along the a axis [4,20], as illustrated in Fig. 1 [3,19]. We consider only nearest-neighbor interactions within the system. By dividing the sites into two sets, we treat the spins as classical vectors. Subsequently, we perform an axis rotation in spin space for sites on the down sublattice to accommodate the classical Néel state, resulting in the magnetic unit cell having twice the volume of the chemical one. The Hamiltonian can thus be reformulated as follows:

$$\mathcal{H}_s = J \sum_{\langle \ell, j \rangle} \left[\frac{1}{2} \left(S_\ell^+ S_j^- + S_\ell^- S_j^+ \right) + \Delta S_\ell^z S_j^z \right], \quad (3)$$

where $S^\pm = S^x \pm iS^y$.

We proceed by employing the zeroth-order expansion of the Holstein-Primakoff transformation [25], which is applicable for the linear spin-wave theory used to investigate spin excitations. Given our focus on modeling the system at very low temperatures, where the population of excited magnons is low, and considering a large number of sites in the system with sizable spin lengths $S = \frac{5}{2}$ for both magnetic sublattices, we use

$$S_\ell^z = b_\ell^\dagger b_\ell - S, \quad S_\ell^+ \simeq \sqrt{2S}\, b_\ell, \quad S_\ell^- \simeq \sqrt{2S}\, b_\ell^\dagger, \quad (4a)$$

$$S_j^z = -b_j^\dagger b_j + S, \quad S_j^+ \simeq \sqrt{2S}\, b_j^\dagger, \quad S_j^- \simeq \sqrt{2S}\, b_j, \quad (4b)$$

where b represents the bosonic operator at the sublattice sites ℓ and j. Upon performing the Fourier transform, the Sm-Fe spin Hamiltonian, up to terms of quadratic order in the
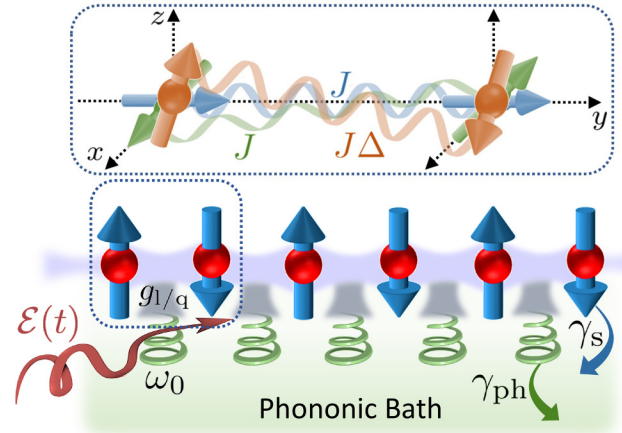

FIG. 1. $SmFeO_3$ at low temperatures considering a spin $S = \frac{5}{2}$ chain with coupling between two magnetic ions, Sm^{3+} and Fe^{3+} [17]. Here, magnetic moments point upwards only when directly neighboring magnetic moments point downwards. The parameter J represents the bare Heisenberg exchange coupling, while Δ quantifies the anisotropy of the spin interactions. Additionally, we model optical phonons using green springs, with ω_0 denoting the phonon frequency and $g_{l/q}$ representing the linear and quadratic spin-phonon coupling. The damping of the driven phonon and the interaction of spins with the phononic bath (other phonons of the system) are, respectively, characterized by the phenomenological rates γ_{ph} and γ_s. Moreover, the steady laser field is represented by $\mathcal{E}(t) = \mathcal{A}_0 \cos(\omega t)$, where $\mathcal{A}_0$ denotes the intensity and ω signifies the frequency.

k space, is expressed as

$$\frac{\mathcal{H}_s}{S} = -LJ\Delta S + J \sum_k [2\Delta b_k^\dagger b_k + \cos(k)(b_k b_{-k} + b_{-k}^\dagger b_k^\dagger)], \quad (5)$$

where L represents the system size or chain length. It is important to note that we neglect the magnon-magnon interaction at very low temperatures. Additionally, for simplicity, we set the lattice constant to 1. To diagonalize the aforementioned spin Hamiltonian, we utilize the bosonic Bogoliubov transformation, employing the operator

$$b_k = \cosh(\theta_k)\mathcal{B}_k + \sinh(\theta_k)\mathcal{B}_{-k}^\dagger \quad (6)$$

with $\sinh(2\theta_k) = -\cos(k)/\sqrt{\Delta^2 - \cos^2(k)}$. Thus, we obtain

$$\frac{\mathcal{H}_s}{S} = \sum_k \varepsilon_k \mathcal{B}_k^\dagger \mathcal{B}_k + \mathcal{E}_0, \quad (7)$$

where ε_k is the magnon dispersion

$$\varepsilon_k = 2J\sqrt{\Delta^2 - \cos^2(k)}, \quad (8)$$

and $\mathcal{E}_0 = \frac{1}{2}\sum_k \varepsilon_k - LJ\Delta(S+1)$ refers to the ground energy.

In the phonon sector, the quadratic SPC arises from the crosstalk between sublattices. Therefore, in our scenario, the optical phonons are expected to originate from the relative movement of ions. Additionally, we assume that the driven noninteracting IR-active phonons are dispersionless, as

described by

$$\mathcal{H}_{\mathrm{ph}} = \omega_0 a_0^\dagger a_0. \tag{9}$$

The phonons are characterized by an energy $\hbar\omega_0$ (we set $\hbar = 1$ throughout the paper), as typically the phonon energy at the phononic band center (corresponding to a dispersionless phonon mode) exceeds the bandwidth of optically dispersive ones in most materials. Conversely, in the case of the usual long-wavelength coupling of laser and phonon, it is evident that the laser will excite modes with very small momentum, making this approximation not far from reality.

In our approach, we aim to locally couple the spins to the phonons for the SPC Hamiltonian. We assume that the relative oscillation of the Sm and Fe ions couples to both the isotropic and anisotropic interactions of spins. The linear and quadratic displacement of an optical phonon modulates the parameters J and Δ, enabling control over the spin system by driving the phonon out of equilibrium. Hence,

$$\mathcal{H}_{\mathrm{s\text{-}ph}}^{\mathrm{iso}} = \sum_{\langle \ell, j \rangle} \sum_{\alpha = x, y} (g_{\mathrm{l}}(a_0^\dagger + a_0) + g_{\mathrm{q}}(a_0^\dagger + a_0)^2)$$
$$\times \left[S_\ell^\alpha S_j^\alpha - \langle S_\ell^\alpha S_j^\alpha \rangle_{\mathrm{eq}} \right], \tag{10a}$$

$$\mathcal{H}_{\mathrm{s\text{-}ph}}^{\mathrm{aniso}} = \sum_{\langle \ell, j \rangle} (g_{\mathrm{l}}\Delta(a_0^\dagger + a_0) + g_{\mathrm{q}}\Delta(a_0^\dagger + a_0)^2)$$
$$\times \left[S_\ell^z S_j^z - \langle S_\ell^z S_j^z \rangle_{\mathrm{eq}} \right], \tag{10b}$$

where g_{l} and g_{q} represent the strengths of the linear and quadratic SPC, respectively. It is worth noting that the isotropic and anisotropic SPCs have units of energy and, for convenience, they are normalized by Δ. The term $\langle \dots \rangle_{\mathrm{eq}}$ denotes subtraction of the equilibrium value of the spin-spin interactions to establish the vacuum state as the ground state of both the phonon and spin sectors. Additionally, since the expectation value of the phonon occupation is proportional to the number of sites ($L = 2501$ in our simulation), the relative quantum fluctuations, proportional to $1/\sqrt{L}$, tend to zero in the thermodynamic limit ($L \to \infty$). Consequently, we employ the mean-field approximation to decouple the SPC acting on the phonon and spin [22], yielding

$$\frac{\mathcal{H}_{\mathrm{s\text{-}ph}}^{\mathrm{MF}}}{S} = \left(g_{\mathrm{l}} \left\langle \frac{a_0^\dagger + a_0}{\sqrt{L}} \right\rangle + g_{\mathrm{q}} \left\langle \frac{a_0^\dagger + a_0}{\sqrt{L}} \right\rangle^2 \right)$$
$$\times \sum_k (\mathcal{T}_k + \mathcal{R}_k [\mathcal{B}_k^\dagger \mathcal{B}_k - \mathcal{N}(\varepsilon_k)]$$
$$+ \mathcal{S}_k [\mathcal{B}_k \mathcal{B}_{-k} + \mathcal{B}_{-k}^\dagger \mathcal{B}_k^\dagger]), \tag{11}$$

where $\mathcal{N}(\varepsilon_k)$ represents the average number of magnons with energy ε_k in equilibrium, and $\mathcal{T}_k$ only influences the ground energy. Additionally, the matrix elements are given by

$$\mathcal{R}_k = \begin{cases} -4J \cos^2(k)/\varepsilon_k & \text{isotropic,} \\ 4J\Delta^2/\varepsilon_k & \text{anisotropic,} \end{cases} \tag{12a}$$

$$\mathcal{S}_k = \begin{cases} 2J\Delta \cos(k)/\varepsilon_k & \text{isotropic,} \\ -2J\Delta \cos(k)/\varepsilon_k & \text{anisotropic.} \end{cases} \tag{12b}$$

Indeed, from Eq. (12), it is apparent that spin excitations occur only when the phonon is coupled to the isotropic and anisotropic interactions separately. Otherwise, $\mathcal{S}_k$ becomes

zero if the phonon is simultaneously coupled to both J and Δ with equal amplitude, indicating the absence of spin excitation in the coupled regime.

Up to this point, we have discussed the undriven Hamiltonian of the system. Now, we introduce the excitation of optical phonons induced by the electric field of the laser [22], which is represented by

$$\mathcal{H}_{\mathrm{lp}} = \mathcal{E}(t)\sqrt{L}(a_0^\dagger + a_0). \tag{13}$$

This setup enables the required excitations to be transferred into the spin chain. It is important to note that when the phonon is driven by the electric field, the discussion of electric field directions pertains to atomic motions. We proceed with a steady laser, given by

$$\mathcal{E}(t) = \mathcal{A}_0 \cos(\omega t), \tag{14}$$

with amplitude (frequency) $\mathcal{A}_0$ (ω). Given our objective of determining the nonequilibrium steady states (NESS) as the desired output, a steady field serves as a suitable input power. While experimental evidence has demonstrated the consideration of the quantum nature of the laser field [26,27], it is typically the case that quantum fluctuations of the laser field are negligible in most experiments, thereby justifying the use of a classical field.

In the following, we define the physical observables of the model for both the spin and phonon subsystems, elucidating how the dynamics can be induced in the magnons by the driven IR-active phonons:

$$q_{\mathrm{ph}}(t) = \left\langle \frac{1}{\sqrt{L}}(a_0^\dagger + a_0) \right\rangle(t), \tag{15a}$$

$$p_{\mathrm{ph}}(t) = \left\langle \frac{i}{\sqrt{L}}(a_0^\dagger - a_0) \right\rangle(t), \tag{15b}$$

$$n_{\mathrm{ph}}(t) = \left\langle \frac{1}{L}a_0^\dagger a_0 \right\rangle(t), \tag{15c}$$

$$\mathcal{Q}_{\mathrm{ph}}(t) = \left\langle \frac{1}{L}(a_0^\dagger a_0^\dagger + a_0 a_0) \right\rangle(t), \tag{15d}$$

$$\mathcal{P}_{\mathrm{ph}}(t) = \left\langle \frac{i}{L}(a_0^\dagger a_0^\dagger - a_0 a_0) \right\rangle(t), \tag{15e}$$

$$n_{\mathrm{s},k}(t) = \langle \mathcal{B}_k^\dagger \mathcal{B}_k \rangle(t), \tag{15f}$$

$$z_{\mathrm{s},k}(t) = \langle \mathcal{B}_{-k}^\dagger \mathcal{B}_k^\dagger \rangle(t), \tag{15g}$$

where, respectively, refer to the phonon displacement, phonon momentum, phonon number, squeezed phonon displacement, squeezed phonon momentum, k component of the spin density, and the k component of off-diagonal excitation (pair magnons). It is also useful to define the total spin density by summing over all k modes; $n_{\mathrm{s}}(t) = \frac{1}{L}\sum_k n_{\mathrm{s},k}(t)$.

To prevent overheating caused by the laser driving, the entire system is coupled to a phononic bath (comprising other undriven phonons of the system). To incorporate the effect of damping due to the coupling to the bath, we utilize the adjoint quantum master equation with phenomenological decay rates for an arbitrary observable $O(t)$ [28,29]. The equation governing the coherent evolution and the dissipator is given
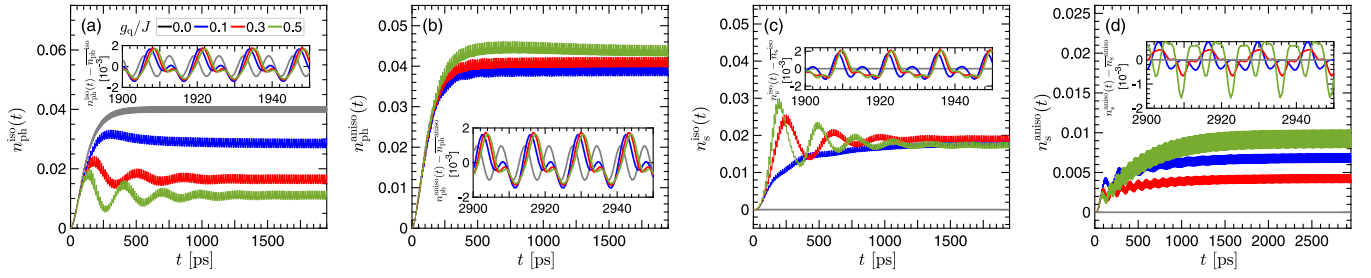
FIG. 2. The dynamics of phonons and magnons are depicted in (a) and (b), respectively, when the laser-driven phonon is exclusively coupled to the isotropic bonds, and in (c) and (d), respectively, when coupled exclusively to the anisotropic bonds in $SmFeO_3$. In the coupled situation, the parameters are set as follows: $\Delta = 1.2$, $\omega = \omega_0 = 2.5J$, $g_1/J = 0.1$, $\mathcal{A}_0/\gamma_{ph} = 0.2$, $\gamma_{ph}/\omega_0 = 0.05$, and $\gamma_s/J = 0.01$. In the decoupled situation, we only have $g_1/J = 0$, $g_q/J = 0$, and $\gamma_s = 0$.

by

$$\langle \dot{O} \rangle(t) = i\langle [\mathcal{H}, O(t)] \rangle + \frac{1}{2} \sum_\ell \gamma_\ell \langle [\mathcal{L}_\ell^\dagger, O(t)] \mathcal{L}_\ell$$

$$+ \mathcal{L}_\ell^\dagger [O(t), \mathcal{L}_\ell] \rangle, \tag{16}$$

where the summation ℓ runs over all possible states in the Hilbert space, and $\mathcal{L}_\ell$ represents the time-independent Lindblad jump operators in the reduced system's Liouville space. The phenomenological decay rates γ_ℓ are γ_s and γ_{ph}, respectively, for the spin and phonon. The first term for the defined $O(t) = \{q_{ph}(t), p_{ph}(t), n_{ph}(t), n_{s,k}(t), z_{s,k}(t) = x_{s,k}(t) + i y_{s,k}(t)\}$ can be straightforwardly calculated. Turning to the second term, the most relevant Lindblad operators are

$$\mathcal{L}_\ell = a_0^\dagger \text{ and } a_0 \mapsto \gamma_\ell = \gamma_{ph} \mathcal{N}(\omega_0) \text{ and } \gamma_{ph}[1 + \mathcal{N}(\omega_0)], \tag{17a}$$

$$\mathcal{L}_\ell = \mathcal{B}_k^\dagger \text{ and } \mathcal{B}_k \mapsto \gamma_\ell = \gamma_s \mathcal{N}(\varepsilon_k) \text{ and } \gamma_s[1 + \mathcal{N}(\varepsilon_k)], \tag{17b}$$

for the phonon and spin, respectively [28]. $\mathcal{N}(\omega_0)$ is the average number of phonon with energy ω_0.

As mentioned before, we assume that both subsystems are in the vacuum state in equilibrium. Additionally, both distributions $\mathcal{N}(\omega_0)$ and $\mathcal{N}(\varepsilon_k)$ vanish at very low temperatures. Taking these into account, we eventually obtain

$$\dot{q}_{ph}(t) = +\omega_0 p_{ph}(t) - \frac{\gamma_{ph}}{2} q_{ph}(t), \tag{18a}$$

$$\dot{p}_{ph}(t) = -\widetilde{\omega}_0(t) q_{ph}(t) - 2\widetilde{\mathcal{E}}(t) - \frac{\gamma_{ph}}{2} p_{ph}(t), \tag{18b}$$

$$\dot{n}_{ph}(t) = -\widetilde{\mathcal{E}}(t) p_{ph}(t) - \frac{1}{2}(\widetilde{\omega}_0(t) - \omega_0)\mathcal{P}_{ph}(t)$$

$$- \gamma_{ph} n_{ph}(t), \tag{18c}$$

$$\dot{\mathcal{Q}}_{ph}(t) = +(\widetilde{\omega}_0(t) + \omega_0)\mathcal{P}_{ph}(t) + 2\widetilde{\mathcal{E}}(t) p_{ph}(t)$$

$$- \gamma_{ph} \mathcal{Q}_{ph}(t), \tag{18d}$$

$$\dot{\mathcal{P}}_{ph}(t) = -(\widetilde{\omega}_0(t) + \omega_0)\mathcal{Q}_{ph}(t) - 2\widetilde{\mathcal{E}}(t) q_{ph}(t)$$

$$- 4g_q\left(2n_{ph}(t) + \frac{1}{L}\right)[\mathcal{N}_s(t) + \mathcal{X}_s(t)]$$

$$- \gamma_{ph} \mathcal{P}_{ph}(t), \tag{18e}$$

$$\dot{n}_{s,k}(t) = +2q_{ph}(t)[g_1 + 2g_q q_{ph}(t)]\mathcal{S}_k y_{s,k}(t) - \gamma_s n_{s,k}(t), \tag{18f}$$

$$\dot{x}_{s,k}(t) = -2\widetilde{\varepsilon}_k(t) y_{s,k}(t) - \gamma_s x_{s,k}(t), \tag{18g}$$

$$\dot{y}_{s,k}(t) = +2\widetilde{\varepsilon}_k(t) x_{s,k}(t) + 2q_{ph}(t)[g_1 + 2g_q q_{ph}(t)]\mathcal{S}_k$$

$$\times \left[n_{s,k}(t) + \frac{1}{2}\right] - \gamma_s y_{s,k}(t), \tag{18h}$$

where $\mathcal{N}_s(t) = \frac{1}{L} \sum_k \mathcal{R}_k n_{s,k}(t)$, $\mathcal{X}_s(t) = \frac{1}{L} \sum_k \mathcal{S}_k x_{s,k}(t)$, and

$$\widetilde{\mathcal{E}}(t) = \mathcal{E}(t) + g_1[\mathcal{N}_s(t) + \mathcal{X}_s(t)], \tag{19a}$$

$$\widetilde{\omega}_0(t) = \omega_0 + 4g_q[\mathcal{N}_s(t) + \mathcal{X}_s(t)], \tag{19b}$$

$$\widetilde{\varepsilon}_k(t) = \varepsilon_k + q_{ph}(t)[g_1 + g_q q_{ph}(t)]\mathcal{R}_k, \tag{19c}$$

respectively, describe the effective electric field in the coupled regime, the dressed phonon frequency, and the dressed magnon dispersion.

III. RESULTS AND DISCUSSION

Depending on the matrix elements $\mathcal{R}_k$ and $\mathcal{S}_k$ defined in Eq. (12), the equations of motion have different solutions for the phonon coupled to isotropic and anisotropic bonds. After solving the tightly coupled equations of motion between subsectors, as a result, magnons acquire dynamics via laser-driven phonons such that the properties of the spin band can be dynamically engineered. We initially examine the regime of on-resonance laser-phonon coupling (LPC) at $\omega = \omega_0$.

First, we consider the case where $g_{1/q} = 0$, i.e., the decoupled phase, where the spin damping is set to zero, $\gamma_s/J = 0$, implying that the magnon density is at its equilibrium value (zero). Numerical solutions indicate that occupations reach the NESS exponentially at around $t \simeq 100$ ps, as depicted by the gray line in Fig. 2(a). Such a short timescale offers applications with higher performance speeds [30]. Regarding $n_{ph}(t)$, Eq. (18c) predicts a timescale of $1/\gamma_{ph}$ from the last damping term. However, one should carefully consider the role of the laser-phonon coupling given by the $\mathcal{E}(t) p_{ph}(t)$ term, leading to an effective timescale of $2/\gamma_{ph}$ at the end to achieve the NESS.

Another noteworthy aspect is the oscillation frequency of $n_{ph}(t)$, which oscillates at twice the frequency $2\omega_0$ in the NESS, frequency-doubling effect, as observed in the inset panels. This phenomenon arises from the laser-phonon coupling term in Eq. (18c). From Fig. 2(a), the time averaging in the NESS for $n_{ph}(t)$ yields $\overline{n_{ph}} = 0.04$. This observation aligns well with elementary electrodynamics, which states that the power of the laser is proportional to the squared

amplitude of the laser field, i.e., $\overline{n_{\text{ph}}} = (\mathcal{A}_0/\gamma_{\text{ph}})^2$. For $\mathcal{A}_0/\gamma_{\text{ph}} = 0.2$ in our simulation, this relationship exhibits excellent agreement.

We now delve into the emergence of (quasi)NESS in the coupled phase, where $g_{l,q} \neq 0$, exhibiting a degree of universality in parameter selection. The magnon dynamics induced by the laser-driven phonon is illustrated in Fig. 2(c). In this scenario, feedback effects between sectors become apparent in the transient processes before reaching the NESS. Here, the phonon pumps into a state lower than the decoupled one, followed by the magnon density of each mode becoming nonzero as a consequence of the same transient feedback, ultimately leading to a spin NESS. The change in the occupation of phonons and magnons with the quadratic SPC is a direct consequence of hybridization effects. With the SPC effects, driving the phonon with a given frequency results in both phonon and magnon exhibiting higher harmonics, as depicted in the inset panels. Similarly, isotropic and anisotropic interactions respond differently to the quadratic SPC. In contrast to J, the occupations coupled to Δ are not strongly affected, as illustrated in Figs. 2(b) and 2(d).

Exciting the IR-active phonons directly with the laser leads to a modulation of both magnetic coupling constants J and Δ, expressed by

$$\tilde{J}(t)/J = 1 + g_l q_{\text{ph,iso}}(t) + g_q q_{\text{ph,iso}}^2(t), \qquad (20\text{a})$$

$$\tilde{\Delta}(t)/\Delta = 1 + g_l q_{\text{ph,aniso}}(t) + g_q q_{\text{ph,aniso}}^2(t). \qquad (20\text{b})$$

As shown, the inclusion of SPCs and linear and quadratic lattice vibrations alters the magnetism of the system. The variance of atomic displacements of a material, represented by squeezed phonon states, can be observed through time-resolved x-ray diffraction peaks in experiments [31], although measuring this variance poses challenges. In Eq. (20), the superscripts "iso" and "aniso" indicate that data are taken with SPC given by $\mathcal{H}_{\text{s-ph}}^{\text{iso}}$ and $\mathcal{H}_{\text{s-ph}}^{\text{aniso}}$, respectively. Note that, since isotropic SPC strongly modifies J while anisotropic SPC strongly modifies only Δ, all data for $\tilde{J}(t)$ [$\tilde{\Delta}(t)$] are obtained using only $\mathcal{H}_{\text{s-ph}}^{\text{iso}}$ ($\mathcal{H}_{\text{s-ph}}^{\text{aniso}}$) throughout this paper.

In general, atomic displacements can influence electronic orbitals, thereby playing a crucial role in shaping the material's electronic structure. Particularly, the distribution of electrons among these orbitals is influenced by the material's chemical potential. Consequently, changes in the material's chemical potential and electronic structure should manifest in spin-orbit coupling and SPCs, if present. Moreover, the density of states describes the distribution of energy states available to electrons in a material, making it directly related to the material's electronic structure. Given that oxygen orbitals influence the bonding between magnetic ions in SmFeO$_3$, SPCs exhibit strong dependence on the material's density of states at the chemical potential [32]. Various static methods, such as temperature, doping, pressure, and electrostatic gating [33–36], have been developed to tune the chemical potential in a controlled manner and induce changes in the coupling constants. Consequently, with the parameters mentioned, experimental manipulation of SPCs enables the detection of phenomena arising from phonon coupling.

Figure 3 illustrates the temporal evolution of J and Δ over short [left part of Figs. 3(a) and 3(b)] to long [right part of
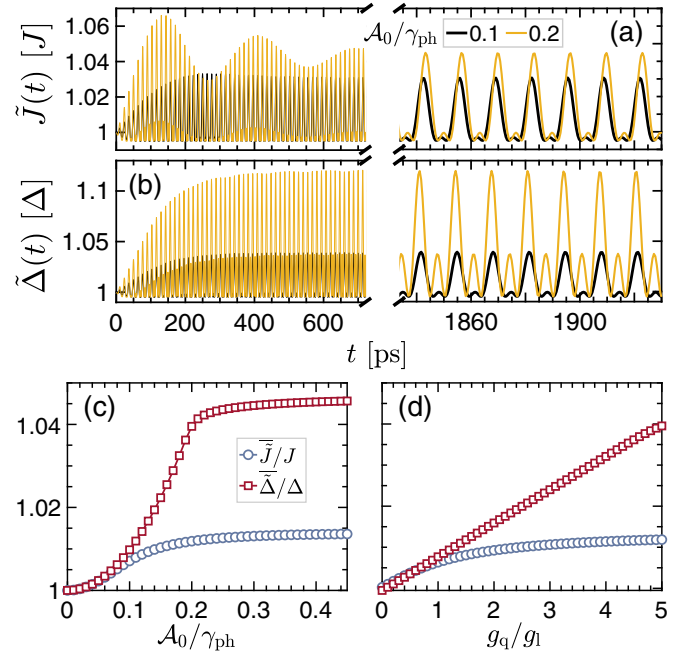

FIG. 3. (a), (b) The temporal evolution of isotropic (J) and anisotropic (Δ) magnetic interactions with a predominant quadratic SPC ($g_q/g_l = 5$) against laser amplitude is depicted. Time averaging in the NESS yields interactions as a function of laser amplitude [(c), with $g_q/g_l = 5$] and SPC [(d), with $\mathcal{A}_0/\gamma_{\text{ph}} = 0.2$]. The intrinsic spin feedback effect in the magnetophononic mechanism results in a saturated spin response to the laser field in the strong coupling regime. Meanwhile, a nonlinear (linear) modulation of the isotropic (anisotropic) response to the SPCs arises due to distinct matrix elements of spin excitations. Parameters: $\omega = \omega_0 = 2.5J$, $\Delta = 1.2$, $\gamma_{\text{ph}}/\omega_0 = 0.05$, and $\gamma_s/J = 0.01$.

Figs. 3(a) and 3(b)] timescales, culminating as the system converges to its long-term steady state around $t \simeq 1000$ ps. In the presence of the laser field, both exchange interactions attain a NESS, characterized by coherent oscillations roughly 5% above the inherent interaction strengths, as depicted in Figs. 3(a) and 3(b). The interaction between spins and phonons becomes evident even in the transient (early-time) dynamics. Notably, the amplitude of oscillations increases with the laser amplitude in both interactions. Additionally, the phase of oscillations in isotropic and anisotropic interactions undergoes slight shifts to the right and left, respectively, owing to a negative sign disparity in the matrix elements of the SPC component. The observed alterations in phonon and magnon occupations, following the modulation of interactions induced by SPC, are direct outcomes of hybridization effects.

Energy transfer occurs from the laser to the spin system until reaching a steady state, altering the effective exchange interactions. As the laser fluence is proportional to $\mathcal{A}_0^2$, one would anticipate J and Δ to scale similarly. This expectation holds up to $\mathcal{A}_0/\gamma_{\text{ph}} = 0.1$ and 0.2, respectively, for J and Δ, but saturates at higher laser intensities. This saturation, illustrated in Fig. 3(c), stems from an inherent spin feedback effect in the strong coupling regime, where spin excitations shift the phonon resonance, hindering further excitations.
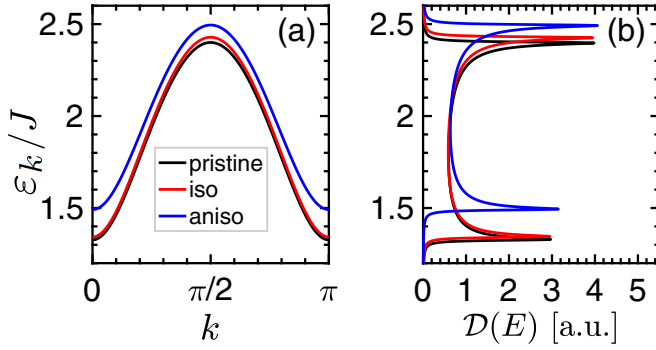
FIG. 4. (a) The plot displays the magnon dispersion, both in its pristine form and after modulation by the laser field. The modulation is particularly evident when the phonon is coupled to either isotropic or anisotropic bonds. (b) Corresponding to these dispersions, it shows the magnonic density of states (in arbitrary units), revealing prominent features associated with band-edge van Hove singularities. These singularities indicate regions where spin excitations are notably enhanced due to the coupling with the laser-driven phonon. Parameters: $\omega = \omega_0 = 2.5J$, $\Delta = 1.2$, $g_q/g_l = 5$, $\mathcal{A}_0/\gamma_{ph} = 0.2$, $\gamma_{ph}/\omega_0 = 0.05$, and $\gamma_s/J = 0.01$.

The data highlight a crucial observation: quadratic SPC significantly alters both isotropic (J) and anisotropic (Δ) magnetic interactions, particularly when the phonon is resonantly driven. This enhanced effect is partly attributed to the stronger impact of linear SPC on the phonon resonance frequency. Thus, driving off resonance might offer a means to even more strongly modify interactions.

Using the modulated interactions, we can elucidate the dynamic evolution of the magnon dispersion under similar conditions. As a result, we establish

$$\varepsilon_k^{\text{iso}} = 2\bar{\bar{J}}\sqrt{\Delta^2 - \cos^2(k)}, \tag{21a}$$

$$\varepsilon_k^{\text{aniso}} = 2J\sqrt{\bar{\bar{\Delta}}^2 - \cos^2(k)}. \tag{21b}$$

The pristine magnon spectrum depicted in Fig. 4(a) illustrates a dispersion ranging from $2\sqrt{\Delta^2 - 1}$ to 2Δ. Upon introducing the laser field, there is a noticeable alteration

in the magnon dispersion, particularly when the phonon is coupled to the isotropic or anisotropic bonds. We can further analyze these changes through the magnonic density of states $\mathcal{D}(E) = (-1/\pi)\text{Im}\sum_k(E + i\eta - \varepsilon_k)^{-1}$, where $\eta/J = 0.001$ serves as a phenomenological broadening parameter. As shown in Fig. 4(b), the resulting density of states reveals prominent features attributed to the band-edge van Hove singularities. These distinctive contributions are expected to manifest in the dynamics of observable quantities.

In many ultrafast experiments, it is common to vary the driving frequencies (ω) to study system dynamics. However, this approach poses challenges and can even lead to dynamical phase transitions in achieving a steady state. To investigate this, we maintain the phonon frequency above the spin band at $\omega_0/J = 2.5$ and vary the laser frequency to explore mutual dressing effects. While SmFeO$_3$ is known to have a strong g_q compared to other quantum magnets, the precise values of g_l and g_q remain unclear. Therefore, we systematically explore parameter space to identify general phenomena.

When $g_q = 0$, the laser electric field acting on the phonon quickly undergoes dressing due to the spin's feedback:

$$\widetilde{\mathcal{E}}(t) = \mathcal{E}(t) + \frac{g_l}{L}\sum_k[\mathcal{R}_k n_{s,k}(t) + \mathcal{S}_k x_{s,k}(t)]. \tag{22}$$

This means that the interaction between the phonon and the laser illustrates the tendency of laser energy to transfer to the magnons. Consequently, the resonance peak at $\omega = \omega_0$ shifts towards lower frequencies due to the nonequilibrium magnon occupation, as depicted in Fig. 5(a).

In the presence of strong linear SPCs, we observe a sudden jump in the isotropic magnetic interaction J at a critical drive frequency ω_c. This jump doubles the strength of J compared to on-resonance modulation and coincides with the creation of a 2% magnon density per site (see the Appendix). Such a jump signifies a dynamical first-order phase transition, similar to the one observed in previous work on a driven fermion chain coupled quadratically to lattice vibrations [23]. However, unlike the dissipation-induced nonlinearity observed in the fermion chain, the phase transition here arises directly from nonlinearity in the mean-field Hamiltonian, driven only by linear SPC. Therefore, the mechanism driving the reported phase
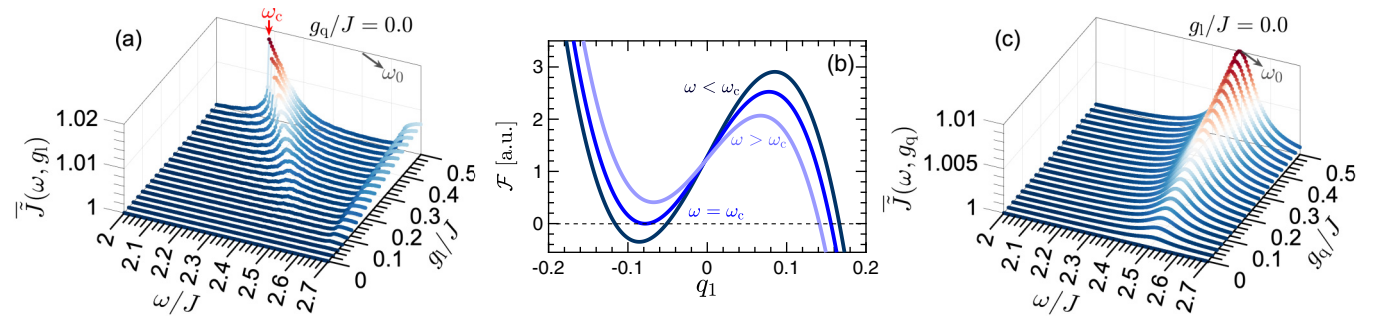

FIG. 5. Dynamical magnetophononic first-order phase transition. (a) The isotropic magnetic interaction plotted against drive frequency for various linear SPCs at $g_q/J = 0.0$. At large g_l, the appearance of the cusp indicates the occurrence of the first-order phase transition. (b) Illustration of the effective force in the NESS acting on the driven-dressed-damped phonon at $g_l/J = 0.5$ and $g_q/J = 0.0$, expanding magnons around the dominant $k = 0$ mode, characterized by the first harmonic of phonon displacement q_1. This confirms the first-order phase transition at ω_c. (c) Similar to (a), but plotted against quadratic SPCs at $g_l/J = 0.0$, demonstrating weak shifts of the phonon resonance, leading to the absence of a phase transition. Parameters: $\omega_0 = 2.5J$, $\Delta = 1.2$, $\mathcal{A}_0/\gamma_{ph} = 0.1$, $\gamma_{ph}/\omega_0 = 0.05$, and $\gamma_s/J = 0.01$.

transition is intrinsic to the spin system, with the drive serving merely as a trigger. The peak near $\omega/J \simeq 2.65$ corresponds to the lower edge of the two-magnon band.

Next, we aim to elucidate the mechanism underlying the emergence of the phase transition in the NESS by examining the dominant harmonic of the driven, dressed, and damped phonons. We construct an effective theoretical framework for understanding the dynamics by approximating the magnons with their single dominant zero-momentum ($k = 0$) mode. To achieve this, we decompose the phonon displacement in the NESS using Fourier decomposition, expressed as $q_{ph}(t) = \overline{q_{ph}} + \sum_{n\neq 0} q_n e^{in\omega t}$, where q_1 represents the dominant first harmonic. For further details, please refer to the Appendix, Sec. 1. This decomposition leads to the following cubic equation:

$$\mathcal{F} = aq_1^3 + bq_1^2 + cq_1 + d = 0, \quad (23)$$

where the hybridized driving, coupling, and damping processes are described by

$$a = 4g_1^2 \mathcal{S}_{k=0}^2 \left[\gamma_s \left(\omega^2 - \omega_0^2 - \frac{\gamma_{ph}^2}{4} \right) + \gamma_{ph}\omega^2 \right], \quad (24a)$$

$$b = -4\mathcal{A}_0\omega_0\gamma_s g_1^2 \mathcal{S}_{k=0}^2, \quad (24b)$$

$$c = \gamma_s \left[\omega^2 - \omega_0^2 - \frac{\gamma_{ph}^2}{4} \right] \left[\omega^2 - 4\varepsilon_{k=0}^2 - \gamma_s^2 \right]$$
$$+ \gamma_{ph}\gamma_s^2\omega^2 - 4\gamma_s g_1^2 \mathcal{S}_{k=0}^2 \omega_0 \varepsilon_{k=0}, \quad (24c)$$

$$d = -\mathcal{A}_0\omega_0\gamma_s \left[\omega^2 - 4\varepsilon_{k=0}^2 - \gamma_s^2 \right]. \quad (24d)$$

Equation (23) can be interpreted as an effective force exerted on the phonon within the driven-coupled-damped regime of the system. To precisely characterize the phase transition, we examine the solution of this equation just before reaching ω_c. The fact that the solutions of the effective force vanish at ω_c serves as evidence for the occurrence of the phase transition, as illustrated in Fig. 5(b). The effective force theory not only elucidates the origin of the transition but also serves as a useful quantitative proxy for determining the exact ω_c.

It is noteworthy that in the vicinity of the first-order phase transition, we observe a rapid initial increase in the dynamics of observables for $t \lesssim 10$ ns. This acceleration is attributed to the heightened magnon density and phonon occupation facilitated by linear SPC, as detailed in the Appendix, Sec. 1. This intriguing behavior suggests the formation of an effective hybridized state on transient timescales, anticipating the phase transition. A similar analysis, applied to the coupling of the phonon to the anisotropic magnetic interaction, yields a dynamical profile somewhat similar to the isotropic case, albeit with the opposite sign due to the presence of quadratic SPC. For a detailed investigation of the impact of another set of parameters, please refer to the Appendix, Sec. 2.

In contrast to the behavior observed with linear SPC, the response of the system to the drive frequency when quadratic SPC dominates reveals a simpler NESS, as shown in Fig. 5(c). In this scenario, no phase transition occurs, at least within the small to intermediate g_q regime. This weaker dynamical response of the nonlinearly coupled spin-phonon system suggests the existence of a quasidecoupled phase, distinct
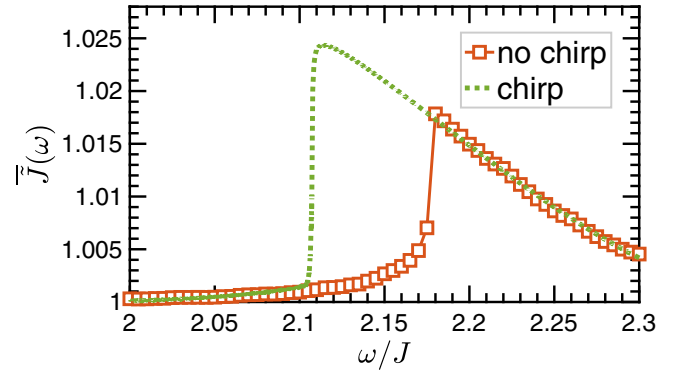

FIG. 6. Chirp protocol for tuning enhancement of magnetism and first-order phase transition in SmFeO₃. Linearly chirped isotropic magnetic interaction with $\mathcal{E}(t)$ from Eq. (25) for $\omega_1/J = 2.3$, $\tau_1 = 500$ ps and $\omega_2/J = 2$, $\tau_2 = 5000$ ps. Employing this chirp enables nearly doubling the size of $\tilde{J}$ compared to the unchirped case before a second transition occurs at $\omega/J = 2.1$. Parameters: $\omega_0 = 2.5J$, $\Delta = 1.2$, $\mathcal{A}_0/\gamma_{ph} = 0.1$, $g_q/J = 0$, $g_1/J = 0.5$, $\gamma_{ph}/\omega_0 = 0.05$, and $\gamma_s/J = 0.01$.

from the nonanalytic response observed in materials driven by quadratic electron-phonon coupling [23,37,38]. Thus, the prevalent quadratic SPC in SmFeO₃ offers opportunities for manipulating the spin band under on-resonance LPC while avoiding phase transitions in off-resonance LPC. However, it is worth noting that the presence of both linear and quadratic SPCs does not prevent the occurrence of the first-order phase transition (see the Appendix).

After discovering the phase transition physics in our model, we are now investigating its applicability in manipulating the magnitude of interaction strength. This exploration is motivated by our recent endeavors in electronic materials research [23]. We consider a linear chirp protocol given by

$$\mathcal{E}^{chirp}(t) = \mathcal{A}_0 \cos \left\{ \omega_1 t + \left[\frac{(\omega_2 - \omega_1)(t - \tau_1)}{\tau_2 - \tau_1} \right] t \right\}, \quad (25)$$

where $\omega_1/J = 2.3$, $\tau_1 = 500$ ps, $\omega_2/J = 2$, and $\tau_2 = 5000$ ps. In this procedure, we gradually decrease the laser frequency from ω_1 to ω_2, passing through the initial phase transition point. This process enables the generation of stronger magnetic interactions, nearly twice the enhancement compared to nonchirped interactions, via a hysteresis loop of adiabatic NESSs, as depicted in Fig. 6. Additionally, it triggers another first-order phase transition at $\omega/J = 2.1$.

IV. EXPERIMENTAL PERSPECTIVE

Continuous driving inevitably results in sample heating, necessitating mitigation of thermal effects [22,23]. To observe nontrivial nonequilibrium spin states, even with relatively modest phonon occupations, sustaining the spin system at low temperatures during prolonged steady driving presents a notable challenge for conventional cold finger cooling capacity. Therefore, incorporating a heat sink with a highly conductive metal becomes essential to efficiently dissipate input power, preventing any thermal bottleneck from occurring due to its thermal contact.
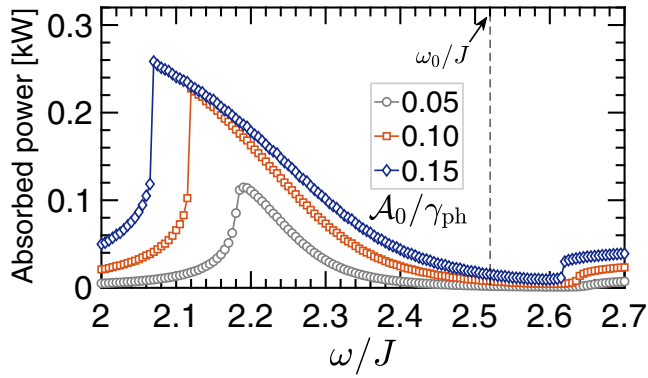
FIG. 7. The absorbed laser power in the NESS for various laser-field amplitudes at low temperatures of the isotropic Hamiltonian exhibits the signature of a nonequilibrium phase transition. This transition occurs due to the competition between energy scales of the system with various laser amplitudes to reach NESS through driving, coupling, and damping mechanisms. Specifically, the first-order phase transition occurs at $\mathcal{A}_0/\gamma_{ph} > 0.05$ for $\Delta = 1.2$, $g_q/J = 0.5$, $g_l/J = 0.5$, $\gamma_{ph}/\omega_0 = 0.05$, and $\gamma_s/J = 0.01$.

We roughly estimate the timescale for reaching the NESS and phase transition. For this purpose, we focus on the dumped power, i.e., the portion of input laser power that directly flows from the driven phonon to the bath, given by $\mathcal{P}_{du}(t) = wa\rho\,\omega_0\gamma_{ph}n_{ph}(t)$. Here, we consider a SmFeO$_3$ sample with a thickness $w = 20$ nm, area $a = 2$ mm^2, and molar density $\rho \simeq 0.028$ mol cm^{-3} [39]. We assume that the sample is in contact with a metal block (heat sink) to absorb thermal energy. The heat sink should be at a low temperature $T \simeq 2$–5 K with a mass $m_b \simeq 2$–5 g and specific heat $C(T) \simeq 1 - 3 \times 10^{-4}$ T J K^{-2} g^{-1} to prevent overheating of the block at the phase transition point with $\overline{n_{ph}^{iso}} \simeq 0.01$. This overheating occurs at

$$t^{heat} = \frac{m_b \int_0^T C(T)\,dT}{\overline{\mathcal{P}_{du}^{iso}}} \simeq 50\,\text{ns}, \tag{26}$$

for the isotropic scenario. This timescale to reach the NESS is significantly longer than the ps timescale obtained in our simulation. Therefore, the computed long-term behavior is readily observable if we have a heat sink to mitigate thermal effects. This implies that the uncovered phase transition can be experimentally detected under these conditions using quantities such as reflectance [40–43]. The advancement of THz drive technology is progressing towards a point where a long-lived monochromatic drive of a single phonon may become feasible. While this might seem ambitious at present, technological advancements suggest that such capabilities could be achievable in the near future.

Additionally, to provide a measurable quantity in the experiment, we consider the NESS energy flow from the drive into the final stage of dissipation for various degrees of freedom. To directly measure the magnetic properties of SmFeO$_3$, we propose the absorbed power

$$\mathcal{P}_{ab}(t) = -wa\rho\,\omega_0\mathcal{E}(t)p_{ph}(t). \tag{27}$$

In Fig. 7, we present a complementary analysis of $\mathcal{P}_{ab}(t)$ in the NESS, reflecting the dynamics induced by the laser field. The persistence of the first-order phase transition for the appropriate laser amplitude at ω_c suggests that the observation of such phenomena is feasible in ultrafast experiments employing the current pump protocol, as the pump effectively transfers sufficient energy to the phononic sector.

V. CONCLUSIONS

In contrast to studies that have relied on equilibrium treatments and static approaches to manipulate the magnetic responses of a system, we propose a dynamical magnetophononic mechanism, modulation of magnetism through phonons, beyond equilibrium. The rare-earth orthoferrite SmFeO$_3$, a functional material in both science and industry, presents potentially unknown features owing to its multiple magnetic orderings associated with an unusual nonlinear spin-phonon coupling. However, its intrinsic magnetic exchange couplings are weak for spintronic applications. To dynamically control the magnetic response of SmFeO$_3$, we apply a continuous laser field. We consider dissipation effects when pumping energy into the system to achieve nonequilibrium steady states at long times. With on-resonance drive of the phonon, inherently weak Sm-Fe magnetic interactions are enhanced, enabling manipulation of the magnonic band, which holds relevance for spintronic applications.

In connection to experimental setups, we probe the system's responses to the pump field when the laser and phonon are purposely chosen to be in the off-resonance regime. This exploration unveils an intriguing phenomenon out of equilibrium, termed as dynamical magnetophononic first-order phase transition. Unlike electron-phonon coupled chains [23,37,38], where the quadratic model exhibits stronger reactions to a pump than the linear model, linear spin-phonon coupling proves sufficient to observe this phenomenon. Moreover, it is more effective than quadratic coupling in enabling phase transitions and engineering magnetic interactions. Finally, we propose a chirp drive protocol to engineer both the first-order phase transition and the enhancement rate of magnetism.
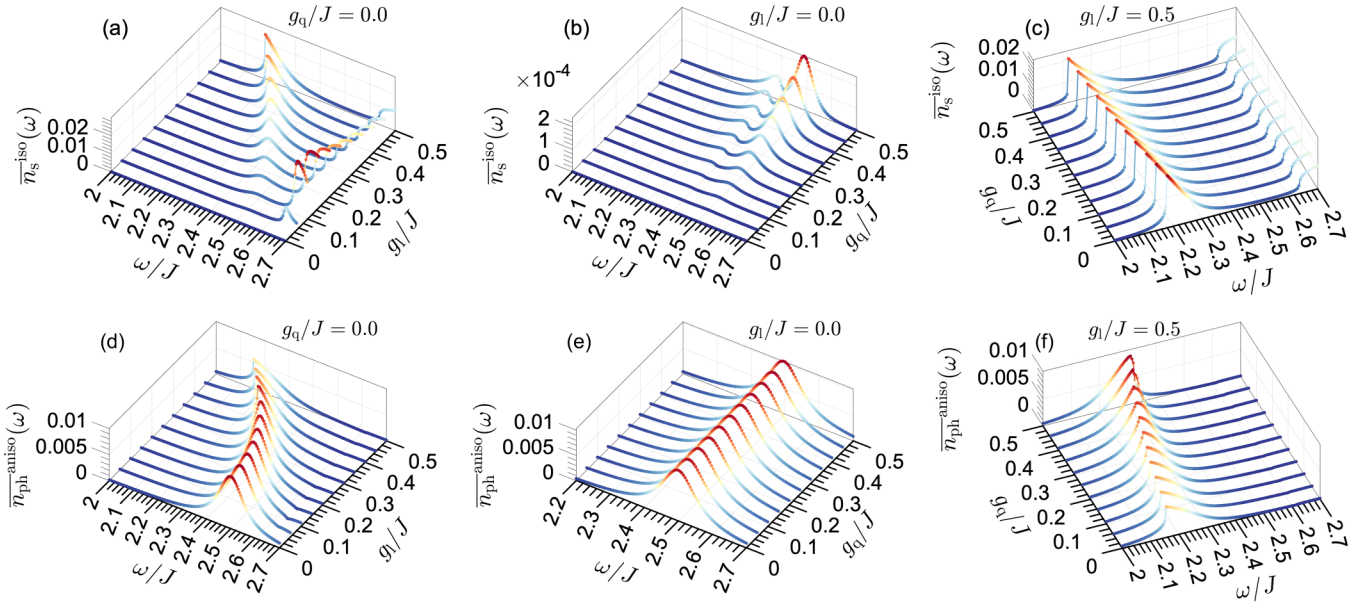
FIG. 8. The phase diagrams for magnon density are depicted in (a) for $g_q = 0$, (b) for $g_l = 0$, and (c) for $g_l = 0.5$. Concurrently, (d)–(f) exhibit the phase diagrams for phonon occupation when phonons are linked to anisotropic bonds (see Fig. 1). Parameters are set as follows: $\Delta = 1.2$, $\omega_0 = 2.5J$, $\mathcal{A}_0/\gamma_{ph} = 0.1$, $\gamma_{ph}/\omega_0 = 0.05$, and $\gamma_s/J = 0.01$.

APPENDIX: DYNAMICAL FIRST-ORDER PHASE TRANSITION IN THE NESS

In this Appendix, we discuss further details surrounding the dynamical first-order phase transition in the NESS, focusing on the perspective of spins. Following this, we provide a comprehensive breakdown of the effective force model introduced in the main body of the text. Additionally, we explore the phononic responses, particularly in cases where phonons interact with anisotropic bonds (see Fig. 1). Lastly, we address how driving, damping, and spin anisotropy influence the first-order phase transition.

Similar to Figs. 5(a) and 5(c) in the main text, in Figs. 8(a)–8(c), we aim to examine the spin response to the drive frequency in the presence of SPCs. When considering only linear SPC, denoted as $g_q = 0$ [see Fig. 8(a)], we observe a notable trend shift in responses towards the critical drive frequency for the phase transition occurrence, mirroring the behavior of phonon occupation. This shift is accompanied by the signature of the van Hove singularity of the two-magnon band around $\omega/J \simeq 2.6$. In the case of only quadratic SPC [see Fig. 8(b)], we similarly observe no significant deviation from the on-resonance response ($\omega = \omega_0 = 2.5$), but the presence of the van Hove singularity of the one-magnon band is evident (with the upper band edge at $\omega/J = 2.4$ for $\Delta = 1.2$). When both linear and quadratic SPCs are present [see Fig. 8(c)], there is a slight shift in the response compared to the scenario with only linear strong SPC, indicating that linear SPC remains dominant for the first-order phase transition in the NESS.

In Figs. 8(d)–8(f), we explore the system's response when the driven IR-active phonons are coupled to the Δ bond as illustrated in Fig. 1, affecting only the z component of spins through the SPC. Despite observing a consistent trend for the phonon occupation akin to Fig. 5(a) of the main text in the presence of sole linear ($g_q = 0$) and quadratic ($g_l = 0$) SPCs, albeit with varying intensities at $g_q = 0$ due to differing matrix elements $\mathcal{R}_k$ in Eq. (12), the presence of both linear and quadratic SPCs in Fig. 8(f) leads to an opposite shift. This shift, complementary to the results obtained in the main text, arises from the negative sign between isotropic and anisotropic matrix elements in Eq. (12). The persistence of the phase transition character of the NESS for the anisotropic SPC implies that most gapped quantum magnets should exhibit the discovered phenomenon when out of equilibrium.

1. Effective force acting on the driven-dressed-damped phonon

In this section, we meticulously derive the effective force acting on the phonon for the coupled dynamics obtained within the Lindblad formalism, focusing on the first harmonic of phonon displacement. We set $g_q = 0$ in the equations of motions since the phase transition originates only from the linear SPC. As discussed in the main text, we consider $q_{ph}(t) = \overline{q_{ph}} + \sum_{n \neq 1} q_n e^{in\omega t}$ in the NESS (valid for arbitrary harmonic n). The time derivative of $q_{ph}(t)$ in the NESS is given by $\dot{q}_{ph}(t) = \sum_n in\omega q_n e^{in\omega t}$. For the product of observables in the equations of motion, we use $A(t)B(t) = \sum_{n,n'} A_{n-n'} B_{n'} e^{in\omega t}$. Considering a single mode $k = 0$ of the spin band edge as the dominant magnon density, we have

$$in\omega q_n = \omega_0 p_n - \frac{\gamma_{ph}}{2} q_n, \tag{A1a}$$

$$in\omega p_n = -\omega_0 q_n - 2\mathcal{A}_0 - 2g_l \mathcal{S}_{k=0} \sum_{n'} x_{s,n'}^{k=0} q_{n-n'} - \frac{\gamma_{ph}}{2} p_n, \tag{A1b}$$
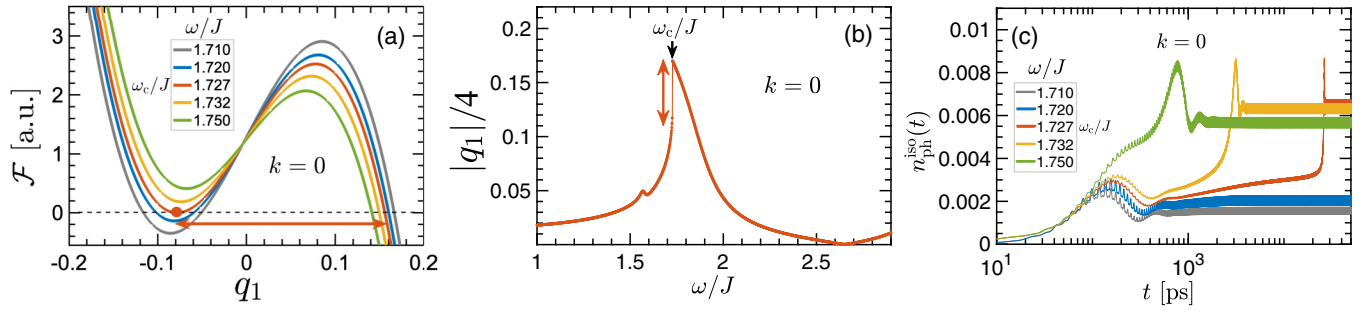
FIG. 9. (a) The effective force in the NESS acting on the driven-dressed-damped phonon is plotted against the first harmonic of phonon displacement q_1. (b) q_1 is depicted against the drive frequency, while (c) illustrates the time evolution of phonon occupation for various drive frequencies. Parameters are set as follows: $\Delta = 1.2$, $\mathcal{A}_0/\gamma_{\mathrm{ph}} = 0.1$, $\gamma_{\mathrm{ph}}/\omega_0 = 0.05$, $\gamma_{\mathrm{s}}/J = 0.01$, $g_1/J = 0.5$, and $g_{\mathrm{q}}/J = 0.0$.

$$0 = 2g_1 \mathcal{S}_{k=0} \sum_{n'} q_{n-n'} y_{\mathrm{s},n}^{k=0} - \gamma_{\mathrm{s}} \overline{n}_{\mathrm{s},k=0}, \tag{A1c}$$

$$in\omega x_{\mathrm{s},n}^{k=0} = -2\varepsilon_{k=0} y_{\mathrm{s},n}^{k=0} - \gamma_{\mathrm{s}} x_{\mathrm{s},n}^{k=0}, \tag{A1d}$$

$$in\omega y_{\mathrm{s},n}^{k=0} = 2\varepsilon_{k=0} x_{\mathrm{s},n}^{k=0} + 2g_1 \mathcal{S}_{k=0} \sum_{n''} \left(n_{\mathrm{s},n''}^{k=0} + 1/2\right) q_{n-n''} - \gamma_{\mathrm{s}} y_{\mathrm{s},n}^{k=0}. \tag{A1e}$$

Invoking dominant harmonics of both phononic and magnonic sectors, i.e., $n = \pm 1$, $n' = \pm 1$, and $n'' = 0$, we find

$$q_{\pm 1} = \frac{2\mathcal{A}_0 \omega_0}{\omega^2 - \omega_0^2 - \frac{\gamma_{\mathrm{ph}}^2}{4} \pm i\gamma_{\mathrm{ph}}\omega - \frac{8g_1^2 \omega_0 \mathcal{S}_{k=0}^2 \varepsilon_{k=0}(\overline{n}_{\mathrm{s},k=0}+1/2)}{\omega^2 - 4\varepsilon_{k=0}^2 - \gamma_{\mathrm{s}}^2 \pm 2i\gamma_{\mathrm{s}}\omega}}, \tag{A2a}$$

$$\overline{n}_{\mathrm{s},k=0} = \frac{2g_1^2 \mathcal{S}_{k=0}^2 (i\omega - \gamma_{\mathrm{s}}) q_1^2}{\gamma_{\mathrm{s}}\left[\omega^2 - 4\varepsilon_{k=0}^2 - \gamma_{\mathrm{s}}^2 - 2i\gamma_{\mathrm{s}}\omega\right] + 4g_1^2 \mathcal{S}_{k=0}^2 (-i\omega + \gamma_{\mathrm{s}}) q_1^2}, \tag{A2b}$$

resulting in a cubic equation for q_1 as

$$4g_1^2 \mathcal{S}_{k=0}^2 \left[\omega^2 - \omega_0^2 - \frac{\gamma_{\mathrm{ph}}^2}{4} + \frac{\gamma_{\mathrm{ph}}}{\gamma_{\mathrm{s}}}\omega^2\right] q_1^3 - 4\mathcal{A}_0 \omega_0 g_1^2 \mathcal{S}_{k=0}^2 q_1^2$$

$$+ \left(\left[\omega^2 - \omega_0^2 - \frac{\gamma_{\mathrm{ph}}^2}{4}\right]\left[\omega^2 - 4\varepsilon_{k=0}^2 - \gamma_{\mathrm{s}}^2\right] + \gamma_{\mathrm{ph}}\gamma_{\mathrm{s}}\omega^2 - 4g_1^2 \mathcal{S}_{k=0}^2 \omega_0 \varepsilon_{k=0}\right) q_1 - \mathcal{A}_0 \omega_0 \left[\omega^2 - 4\varepsilon_{k=0}^2 - \gamma_{\mathrm{s}}^2\right] = 0, \tag{A3}$$

where we have taken only the real parts of the coefficients to align with the numerical results. This equation yields three solutions when we set it equal to $\mathcal{F} = 0$, which behaves as an effective force acting on the phonon after applying drive, coupling to the magnon, and damping to the phononic bath. Tracking the solutions of this force in Fig. 9(a) for different drive frequencies and using the same parameter set as in the main text, we observe three distinct regions: $\omega < \omega_{\mathrm{c}}$, $\omega = \omega_{\mathrm{c}}$, and $\omega > \omega_{\mathrm{c}}$, where ω_{c} denotes the critical driving frequency at which the phase transition occurs. For $\omega < \omega_{\mathrm{c}}$, three roots appear for the force as a function of q_1, indicated by dark gray and blue lines. For $\omega > \omega_{\mathrm{c}}$, a single root emerges, as shown by yellow and green lines, while for $\omega = \omega_{\mathrm{c}}$, two of the roots become identical, resulting in the minimization of the absolute value of the force. This effect is confirmed by observing that the first-order phase transition in our numerical

q_1 [see Fig. 9(b)] perfectly matches ω_{c} obtained from the force model, even the difference between roots in the minimized force corresponds to the cusp height in q_1.

To delve into the real-time dynamics further, the time evolution of the expectation values of the phonon occupation for the same drive frequencies confirms the sharp transition of transient dynamics in the strong coupling regime, where a sharp spike emerges at long times, as depicted in Fig. 9(c).

As mentioned in the main text, this effective force accurately represents both qualitatively and quantitatively the phase transition observed in the numerical results. At ω_{c}, setting the imaginary parts of the second and third solutions of the above equation to zero yields an analytical expression for ω_{c} as a function of all parameters. After this step, we obtain a drive frequency that satisfies the condition of zero imaginary part for the second or third solutions, given by

$$\omega_i^2 = \frac{\omega_0^2(1 - \gamma_{\mathrm{s}}) - 4\omega^2 + \sqrt{\omega_0^4(1 - 2\gamma_{\mathrm{s}} - 4\gamma_{\mathrm{ph}}\gamma_{\mathrm{s}}) + 16\varepsilon_{k=0}^4 + 8\omega_0^2 \varepsilon_{k=0}^2 (1 - \gamma_{\mathrm{s}} - 2\gamma_{\mathrm{ph}}\gamma_{\mathrm{s}})}}{2(\gamma_{\mathrm{s}} - \gamma_{\mathrm{ph}})}. \tag{A4}$$
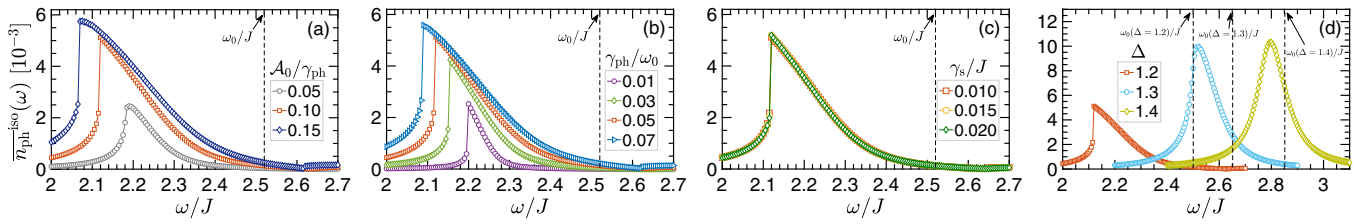
FIG. 10. The influence of model parameters on the dynamical first-order phase transition: (a) The impact of driving with parameters set to $\Delta = 1.2$, $\gamma_{\mathrm{ph}}/\omega_0 = 0.05$, and $\gamma_{\mathrm{s}}/J = 0.01$. (b) The effect of phonon damping characterized by $\Delta = 1.2$, $\mathcal{A}_0/\gamma_{\mathrm{ph}} = 0.1$, and $\gamma_{\mathrm{s}}/J = 0.01$. (c) The influence of spin damping under conditions of $\Delta = 1.2$, $\mathcal{A}_0/\gamma_{\mathrm{ph}} = 0.1$, and $\gamma_{\mathrm{ph}}/\omega_0 = 0.05$. (d) The impact of spin anisotropy described by $\mathcal{A}_0/\gamma_{\mathrm{ph}} = 0.1$, $\gamma_{\mathrm{ph}}/\omega_0 = 0.05$, and $\gamma_{\mathrm{s}}/J = 0.01$.

Having ω_i, $q_1 = \frac{\mathcal{A}_0 \omega_0 \gamma_{\mathrm{s}} g_1^2 \mathcal{S}_{k=0}^2}{3 g_1^2 \mathcal{S}_{k=0}^2 [\gamma_{\mathrm{s}}(\omega_i^2 - \omega_0^2 - \gamma_{\mathrm{ph}}^2/4) + \gamma_{\mathrm{ph}}\omega_i^2]}$ is obtained. Plugging this q_1 into Eq. (A3) at $\omega = \omega_{\mathrm{c}}$, the critical drive frequency can easily be achieved.

2. Effect of driving, damping, and spin anisotropy on the dynamical first-order phase transition

To investigate the influence of model parameters on the observed first-order phase transition, we present in Fig. 10 a scan of the drive amplitude, phonon damping, spin damping, and spin anisotropy. Given that the observables considered in the model consistently reach long-time plateaus, the trend of the phonon occupation response to various drive amplitudes should mirror the absorbed power as shown in Figs. 10(a) and 6 of the main text.

However, it is appropriate to inquire whether the phase transition alters in the long-time steady state when phonon damping becomes weaker or stronger, as illustrated in Fig. 10(b). Our analysis reveals that the first-order phase transition occurs across most phonon damping rates, indicating that the spin damping [Fig. 10(c)] does not significantly influence tuning the critical drive frequency. This suggests that the transition remains independent of the value of γ_{s}. This can be understood from the analysis of the effective force acting on the phonon, where the contribution from terms involving spin damping is negligible due to the assumption of a weak damping regime.

Finally, we explore the impact of spin anisotropy in Fig. 10(d), considering various spin anisotropies with corresponding phonon energies $\omega_0 > 2J\Delta$. With the ability to tune the spin rotation symmetry through $\Delta > 1$, resulting in an increased gap size in the magnon dispersion, we do not observe the first-order phase transition for the same parameter set. However, one would anticipate observing it with different parameters, such as a stronger laser field being necessary to observe the transition when Δ becomes larger.

[1] Z. Zheng and J. E. Greedan, *Rare Earth Elements and Materials* (Academic, New York, 2003).

[2] X. Li, D. Kim, Y. Liu, and J. Kono, Terahertz spin dynamics in rare-earth orthoferrites, Photonics Insights **1**, R05 (2022).

[3] M. C. Weber, M. Guennou, D. M. Evans, C. Toulouse, A. Simonov, Y. Kholina, X. Ma, W. Ren, S. Cao, M. A. Carpenter, B. Dkhil, M. Fiebig, and J. Kreisel, Emerging spin–phonon coupling through cross-talk of two magnetic sublattices, Nat. Commun. **13**, 443 (2022).

[4] D. Amoroso, B. Dupé, and M. J. Verstraete, Unraveling the role of Sm $4f$ electrons in the magnetism of SmFeO₃, Phys. Rev. B **107**, 104427 (2023).

[5] E. Bousquet and A. Cano, Non-collinear magnetism in multiferroic perovskites, J. Phys.: Condens. Matter **28**, 123001 (2016).

[6] H. Liu and X. Yang, A brief review on perovskite multiferroics, Ferroelectrics **507**, 69 (2017).

[7] M. Fiebig, T. Lottermoser, D. Meier, and M. Trassin, The evolution of multiferroics, Nat. Rev. Mater. **1**, 16046 (2016).

[8] N. A. Spaldin, S.-W. Cheong, and R. Ramesh, Multiferroics: Past, present, and future, Phys. Today **63**(10), 38 (2010).

[9] N. A. Spaldin, Multiferroics: Past, present, and future, MRS Bull. **42**, 385 (2017).

[10] N. Suresh Kumar and K. Chandra Babu Naidu, A review on perovskite solar cells (PSCs), materials and applications, J. Materiomics **7**, 940 (2021).

[11] T. Wu, Z. Qin, Y. Wang, Y. Wu, W. Chen, S. Zhang, M. Cai, S. Dai, J. Zhang, J. Liu, Z. Zhou, X. Liu, H. Segawa, H. Tan, Q. Tang, J. Fang, Y. Li, L. Ding, Z. Ning, Y. Qi *et al.*, The main progress of perovskite solar cells in 2020–2021, Nano-Micro Lett. **13**, 152 (2021).

[12] A. V. Kimel, A. Kirilyuk, P. A. Usachev, R. V. Pisarev, A. M. Balbashov, and T. Rasing, Ultrafast non-thermal control of magnetization by instantaneous photomagnetic pulses, Nature (London) **435**, 655 (2005).

[13] M. E. Zayed, C. Rüegg, J. Larrea, J. A. M. Läuchli, C. Panagopoulos, S. S. Saxena, M. Ellerby, D. F. McMorrow, T. Strässle, S. Klotz, G. Hamel, R. A. Sadykov, V. Pomjakushin, M. Boehm, M. Jiménez-Ruiz, A. Schneidewind, E. Pomjakushina, M. Stingaciu, K. Conder, and H. M. Rønnow, 4-spin plaquette singlet state in the Shastry–Sutherland compound SrCu₂(BO₃)₂, Nat. Phys. **13**, 962 (2017).

[14] J. Romhányi, K. Penc, and R. Ganesh, Hall effect of triplons in a dimerized quantum magnet, Nat. Commun. **6**, 6805 (2015).

[15] D. Afanasiev, J. R. Hortensius, B. A. Ivanov, A. Sasani, E. Bousquet, Y. M. Blanter, R. V. Mikhaylovskiy, A. V. Kimel,

and A. D. Caviglia, Ultrafast control of magnetic interactions via light-driven phonons, Nat. Mater. **20**, 607 (2021).

[16] D. Bossini, M. Pancaldi, L. Soumah, M. Basini, F. Mertens, M. Cinchetti, T. Satoh, O. Gomonay, and S. Bonetti, Ultrafast amplification and nonlinear magnetoelastic coupling of coherent magnon modes in an antiferromagnet, Phys. Rev. Lett. **127**, 077202 (2021).

[17] S. Chaturvedi, P. Shyam, A. Apte, J. Kumar, A. Bhattacharyya, A. M. Awasthi, and S. Kulkarni, Dynamics of electron density, spin-phonon coupling, and dielectric properties of $SmFeO_3$ nanoparticles at the spin-reorientation temperature: Role of exchange striction, Phys. Rev. B **93**, 174117 (2016).

[18] M. Fechner, A. Sukhov, L. Chotorlishvili, C. Kenel, J. Berakdar, and N. A. Spaldin, Magnetophononics: Ultrafast spin control through the lattice, Phys. Rev. Mater. **2**, 064401 (2018).

[19] S. Cao, H. Zhao, B. Kang, J. Zhang, and W. Ren, Temperature induced spin switching in $SmFeO_3$ single crystal, Sci. Rep. **4**, 5960 (2014).

[20] D. R. Baykusheva, M. H. Kalthoff, D. Hofmann, M. Claassen, D. M. Kennes, M. A. Sentef, and M. Mitrano, Witnessing nonequilibrium entanglement dynamics in a strongly correlated fermionic chain, Phys. Rev. Lett. **130**, 106902 (2023).

[21] R. J. Glauber, Coherent and incoherent states of the radiation field, Phys. Rev. **131**, 2766 (1963).

[22] M. Yarmohammadi, C. Meyer, B. Fauseweh, B. Normand, and G. S. Uhrig, Dynamical properties of a driven dissipative dimerized $S = \frac{1}{2}$ chain, Phys. Rev. B **103**, 045132 (2021).

[23] M. Yarmohammadi, M. Bukov, and M. H. Kolodrubetz, Nonequilibrium phononic first-order phase transition in a driven fermion chain, Phys. Rev. B **108**, L140305 (2023).

[24] M. Yarmohammadi, M. Krebs, G. S. Uhrig, and B. Normand, Strong-coupling magnetophononics: Self-blocking, phonon-bitriplons, and spin-band engineering, Phys. Rev. B **107**, 174415 (2023).

[25] T. Holstein and H. Primakoff, Field dependence of the intrinsic domain magnetization of a ferromagnet, Phys. Rev. **58**, 1098 (1940).

[26] G. Mazza and A. Georges, Superradiant quantum materials, Phys. Rev. Lett. **122**, 017401 (2019).

[27] M. A. Sentef, M. Ruggenthaler, and A. Rubio, Cavity quantum-electrodynamical polaritonically enhanced electron-phonon coupling and its influence on superconductivity, Sci. Adv. **4**, eaau6969 (2018).

[28] H. Breuer and F. Petruccione, *The Theory of Open Quantum Systems* (Oxford University Press, Oxford, 2007).

[29] G. Lindblad, On the generators of quantum dynamical semigroups, Commun. Math. Phys. **48**, 119 (1976).

[30] D. N. Basov, R. D. Averitt, and D. Hsieh, Towards properties on demand in quantum materials, Nat. Mater. **16**, 1077 (2017).

[31] S. L. Johnson, P. Beaud, E. Vorobeva, C. J. Milne, E. D. Murray, S. Fahy, and G. Ingold, Directly observing squeezed phonon states with femtosecond x-ray diffraction, Phys. Rev. Lett. **102**, 175503 (2009).

[32] E. van Heumen, M. Berben, L. Neubrand, and Y. Huang, Scattering rate collapse driven by a van hove singularity in the dirac semimetal $PdTe_2$, Phys. Rev. Mater. **3**, 114202 (2019).

[33] R. Mori, P. B. Marshall, K. Ahadi, J. D. Denlinger, S. Stemmer, and A. Lanzara, Controlling a van hove singularity and fermi surface topology at a complex oxide heterostructure interface, Nat. Commun. **10**, 5534 (2019).

[34] J. Zhang, P. W. Hess, A. Kyprianidis, P. Becker, A. Lee, J. Smith, G. Pagano, I.-D. Potirniche, A. C. Potter, A. Vishwanath, N. Y. Yao, and C. Monroe, Observation of a discrete time crystal, Nature (London) **543**, 217 (2017).

[35] S. Sen and G.-Y. Guo, Pressure induced lifshitz transition in ThFeAsN, Phys. Rev. Mater. **4**, 104802 (2020).

[36] G. Singh, A. Jouan, G. Herranz, M. Scigaj, F. Sánchez, L. Benfatto, S. Caprara, M. Grilli, G. Saiz, F. Couëdo, C. Feuillet-Palma, J. Lesueur, and N. Bergeal, Gap suppression at a lifshitz transition in a multi-condensate superconductor, Nat. Mater. **18**, 948 (2019).

[37] J. Sous, B. Kloss, D. M. Kennes, D. R. Reichman, and A. J. Millis, Phonon-induced disorder in dynamics of optically pumped metals from nonlinear electron-phonon coupling, Nat. Commun. **12**, 5803 (2021).

[38] D. M. Kennes, E. Y. Wilner, D. R. Reichman, and A. J. Millis, Transient superconductivity from electronic squeezing of optically pumped phonons, Nat. Phys. **13**, 479 (2017).

[39] $SmFeO_3$ crystal structure: Data sheet from "Pauling file multinaries edition 2022" in SpringerMaterials database.

[40] A. von Hoegen, M. Fechner, M. Först, N. Taherian, E. Rowe, A. Ribak, J. Porras, B. Keimer, M. Michael, E. Demler, and A. Cavalleri, Amplification of superconducting fluctuations in driven $YBa_2 Cu_3 O_{6+x}$, Phys. Rev. X **12**, 031008 (2022).

[41] M. Buzzi, D. Nicoletti, M. Fechner, N. Tancogne-Dejean, M. A. Sentef, A. Georges, T. Biesner, E. Uykur, M. Dressel, A. Henderson, T. Siegrist, J. A. Schlueter, K. Miyagawa, K. Kanoda, M.-S. Nam, A. Ardavan, J. Coulthard, J. Tindall, F. Schlawin, D. Jaksch *et al.*, Photomolecular high-temperature superconductivity, Phys. Rev. X **10**, 031028 (2020).

[42] M. Buzzi, G. Jotzu, A. Cavalleri, J. I. Cirac, E. A. Demler, B. I. Halperin, M. D. Lukin, T. Shi, Y. Wang, and D. Podolsky, Higgs-mediated optical amplification in a nonequilibrium superconductor, Phys. Rev. X **11**, 011055 (2021).

[43] M. Buzzi, D. Nicoletti, S. Fava, G. Jotzu, K. Miyagawa, K. Kanoda, A. Henderson, T. Siegrist, J. A. Schlueter, M.-S. Nam, A. Ardavan, and A. Cavalleri, Phase diagram for light-induced superconductivity in κ-$(ET)_2$-X, Phys. Rev. Lett. **127**, 197002 (2021).